CrossMark

ORIGINAL PAPER

DFT/TDDFT computational study of the structural, electronic and optical properties of rhodium (III) and iridium (III) complexes based on tris-picolinate bidentate ligands

Houari Brahim[1] · Boumediene Haddad[1] · Sefia Brahim[1] · Abdelkrim Guendouzi[1]

Abstract The electronic structures and spectroscopic properties of two complexes $[M(pic)_3]$ (M = Ir, Rh) containing picolinate as bidentate ligands have been calculated by means density functional theory (DFT) and time-dependent DFT/ TD-DFT using three hybrid functionals B3LYP, PBE0 and mPW1PW91. The PBE0 and mPW1PW91 functionals, which have the same HF exchange fraction (25%), give similar results and do not differ drastically from B3LYP results. Calculated geometric parameters of the complexes are in good agreement with the available experimental data. The UV absorptions observed in acetonitrile were assigned on the basis of singlet state transitions. The most intense band observed in the UV-C region corresponds to ligand-to-ligand charge transfer states (LLCT) in both complexes. The theoretical spectrum of the rhodium complex is characterized by a large degree of mixing between metal-to-ligand-charge-transfer (MLCT), LLCT and metal centered (MC) states in the UV-A region. The presence of low-lying excited states with MC character affects the absorption spectrum under spin-orbit coupling (SOC) effects and play important roles in the photochemical properties.

Keywords TD-DFT · Rhodium · Iridium complexes · Absorption spectrum · Picolinate · MLCT · Bidentate ligands

✉ Houari Brahim
  brahim.h@outlook.com

[1] Department of Chemistry, Dr Moulay Tahar University of Saida, 20000 Saida, Algeria

Introduction

In the last decade, cyclometalated rhodium (III) and iridium (III) complexes have attracted much attention and have been studied extensively in both experimental and theoretical areas [1–3]. This interest is due to their rich applications in many fields: as catalyst supports [4, 5], in the fields of organic light-emitting diodes OLED [6–9], as antimicrobial agents in biological activities [10], and as candidates for anticancer agents [11, 12].

At the molecular level, the relationship between the ligands and the metal centers is known to govern the electrochemical, photophysical and luminescence properties of cyclometalated complexes. Most studies to date have focused on understanding the electronic communication in these complexes, Examples include cyclometalated rhodium(III) and iridium(III) complexes with imidazolyl modified phenanthroline ligands [13], containing picolinate as bidentate ligands as an N,O-chelating ligand [14–16], and the [bis(2-phenylpyridine)(2-carboxy-4-dimethylaminopyridine)] iridium(III) complex with picolinate ligand [17].

Also, a comprehensive report by Minaev et al. [17] stated that the introduction of two F atoms at specific positions of the ppy ligands, in combination with the employment of picolinate as an ancillary ligand, provides a very efficient blue-emitting bis-cyclometalated dye [18]. Recently, Ko et al. [19] reported that exchanging the acetylacetonate ancillary ligand for a picolinate one has a major impact on the phosphorescent properties of platinum complexes. In order to find new complexes for biological applications, Basu and co-workers [20] synthesized two complexes of rhodium and iridium containing tris-picolinate ligands $[M(pic)_3]$ (M = Ir, Rh). In both complexes, the picolinate ligands are coordinated to the metal center as bidentate N- and O-donors forming five-membered chelate rings. In the paper cited above, the

Springer

structural, spectroscopic and electrochemical properties of the two complexes were investigated. The experimental electronic spectrum of each complex showed several intense absorptions below 400 nm. The authors suggested that the lowest energy absorption (370 nm) is probably due to a metal-to-ligand charge transfer (MLCT) transition, and that the other absorptions observed at higher energies correspond to and ligand-to-ligand charge transfer (LLCT) transitions. Extended Hückel Molecular Orbital (EHMO) calculations have been used to explore the composition of some frontier molecular orbitals (FMOs), and it was found that the first three occupied orbitals are relatively close, and have major contributions from d metal orbitals in the two complexes. However this method is not recommended for this type of calculation, thus the use of advanced quantum chemistry methods is necessary.

In the present work, we studied theoretically the geometric structures, frontier molecular orbital (FMO) character, energy gaps and UV/IR spectra of $[M(pic)_3]$ (M = Ir (1), Rh (2)) by density functional theory (DFT) and time-dependent DFT (TD-DFT) calculations. The theoretical results are compared with experimental data.

Computational details

The singlet ground states S_0 of 1-2 complexes were optimized using DFT with three hybrid functionals, B3LYP [21–23], PBE0 [24] and mPW1PW91 [25], combined with the 6-311 + G(d,p) [26–28] basis set for the non-metal atoms and a double-ζ quality basis set LANL2DZ [29, 30] for the metal atoms iridium and rhodium. The optimizations were performed in solution (acetonitrile, $\varepsilon = 35.688$) using X-ray structures [20] as starting geometries without any constraint. Solvent effect was calculated using polarizable continuum model (PCM) [31, 32]. Vibrational frequency analyses were performed to confirm that the optimized structures were a true minimum, and to calculate infrared spectra. UV-vis spectra were studied using the TD-DFT method [33–35] on the basis of optimized ground states with the same functionals and basis sets. We used the Gaussian 09 program package [36] to perform all calculations, Gaussum-3 [37] to simulate and analyze electronic and infrared spectra, Avogadro-1 [38] to get orbital isosurfaces and Ortep-3 [39] to visualizing geometric structures.

Results and discussion

Geometry of the electronic ground state

The structures of the complexes facial (fac-) and meridional (mer-) isomers of $[M(pic)_3]$ (M = Ir (1), Rh (2)) (Scheme 1)

were fully optimized using three hybrid functionals PBE0, mPW1PW91 and B3LYP in acetonitrile. The bond distances and bond angles of main structural parameters are reported in Table 1 together with experimental data obtained from X-ray crystallographic study [20]. The results show that mer-$M(pic)_3$ isomers (C_1 symmetry) of both iridium and rhodium complexes are more stable than fac-$M(pic)_3$ isomers (C_3 symmetry) ($\Delta E \approx 15.43$ kJ mol^{-1} calculated with PBE0). These results agree with ^{1}H NMR spectra, which clearly show the absence of any C_3 symmetry in the complex molecules and thus indicate that the meridional stereochemistry prevails in solution for both complexes.

Therefore, we will study only the mer-$M(pic)_3$ isomers of complexes 1 and 2. As shown in Scheme 1, the Rh(III) and Ir(III) complexes present a pseudo-octahedral coordination around the rhodium and iridium centers owing to the $4d^6$ and $5d^6$ electronic configuration of Rh^{+3} and Ir^{+3} cation, respectively, both centers metals are coordinated by three nitrogen and three oxygen atoms from picolinate ligands.

According to Table 1, we noted that, for both complexes, unlike PBE0 and mPW1PW91 functionals, the B3LYP functional overestimates the bond lengths and therefore is not reliable in predicting the structure of iridium (III) and rhodium (III) complexes. The mPW1PW91 functional gives slightly larger Ir–O and Ir–N bond lengths than the PBE0 functional. The B3LYP functional gives better bond distances than the PBE0 and mPW1PW91 functionals if we exclude the C(13)–O(6) bond length. The coordination of both metal centers to the three nitrogens is characterized by calculated M–N(1) and M–N(2) bond lengths significantly shorter than the corresponding M–N(3) bond lengths; for example, M–N(1) and M–N(2) bond lengths for M = Rh, Ir are 2.039 and 2.028 Å, respectively, much shorter than M–N(3) bond (2.048 Å). This indicates that the interaction between the N(1) and N(2) of the picolinate ligand and the metal center is stronger than the one between the N(3) ligand and the metal center.

For example, the experimental bond length of mer-Ir(pic)$_3$ Ir–N(2) = 2.026 Å, which is well reproduced both by PBE0 (2.025 Å) and mPW1PW91 functionals (2.028 Å), while a mean difference of 0.026 Å is obtained by B3LYP.

In the case of the bond angles, a similar trend is obtained, e.g.; the experimental and theoretical values agree rather well for the bond-angles N(1)–M–O(1), N(3)–M–O(5) and N(1)–M–N(3) (M = Rh, Ir). For N(2)–M–O(3), N(2)–M–O(5) and O(1)–M–O(3), there is a mean difference between the theoretical values and the experimental values. PBE0 and mPW1PW91 functionals gives better N(1)–M–O(1), N(3)–M–O(5) and N(1)–M–N(3) (M = Rh, Ir) bond angles than the B3LYP functional with respect to the experimental data.

Substituting the metal center by a chromium atom, resulting in Cr(pic)$_3$ complex, the X-ray experimental structure has been obtained by Hakimi [40], give Cr–

Scheme 1 Geometric structure of **a** meridional (mer)-M(pic)₃ and **b** facial (fac)-M(pic)₃ with M = Ir, Rh

(a) *mer*-**M(pic)₃**   (b) *fac*-**M(pic)₃**
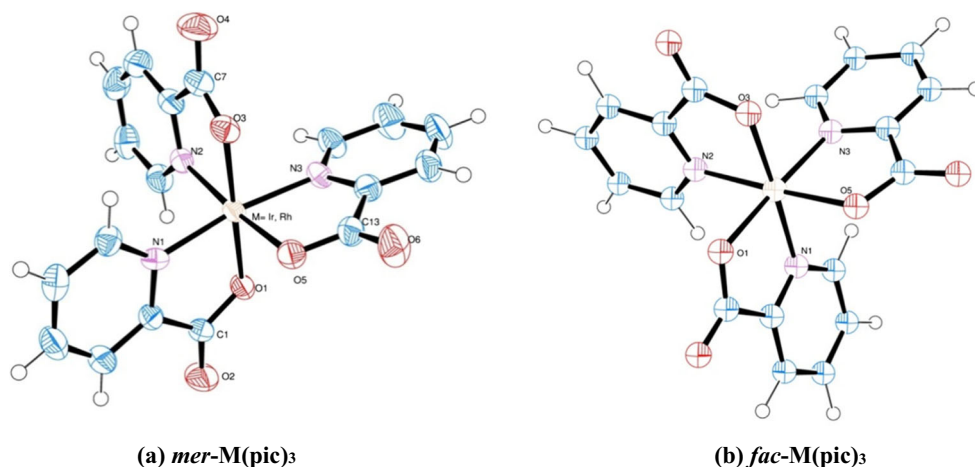
N bond lengths longer (2.045–2.063 Å) than the Ir–N bonds (2.014–2.039 Å) and Rh–N bonds (2.011–2.028 Å). This points to the crucial role of the central metal atom in the ligand coordination, namely increasing the electronegativity difference between the center metal and the donor atom of the picolinate ligands [Cr (1.66) < Ir (2.25) < Rh (2.28)], leads to a decrease in bond lengths.

Further inspection shows that, in mer-M(pic)₃ complexes, upon going from B3LYP, mPW1PW91 to PBE0.

the calculated M–N bond distances slightly decrease, except for Rh–N(2) in the mer-Rh(pic)₃ complex. On the whole, the agreement between structural results is particularly good with the hybrid functionals PBE0 and mPW1PW91. These results are consistent with those reported by Li et al. [41] in (Py-BTE)₂Ir(acac) complex, and Nie et al. [42]; these latter authors strongly recommend the application of mPW1PW91 level instead of B3LYP for the prediction of the electronic spectra, especially for ground state geometries.

Table 1 Selected optimized bond lengths (in Å) and bond angles (in °) of meridional (mer)-Ir(pic)₃ and mer-Rh(pic)₃

	mer-Ir(pic)₃				mer-Rh(pic)₃			
	mPW1PW91	B3LYP	PBE0	X-ray[a]	mPW1PW91	B3LYP	PBE0	X-ray[a]
Bond distances								
M–N(1)	2.039	2.061	2.036	2.014(4)	2.036	2.060	2.025	2.011(4)
M–N(2)	2.028	2.052	2.025	2.026(5)	2.037	2.063	2.043	2.017(4)
M–N(3)	2.048	2.071	2.045	2.039(4)	2.048	2.073	2.044	2.028(4)
M–O(1)	2.055	2.076	2.053	2.033(4)	2.037	2.059	2.034	2.022(3)
M–O(3)	2.060	2.082	2.059	2.042(4)	2.044	2.066	2.051	2.013(3)
M–O(5)	2.057	2.076	2.056	2.037(4)	2.036	2.055	2.017	2.025(3)
C(1)–O(1)	1.298	1.305	1.298	1.309(6)	1.296	1.303	1.299	1.306(6)
C(1)–O(2)	1.215	1.220	1.215	1.207(7)	1.216	1.220	1.210	1.203(6)
C(7)–O(3)	1.298	1.305	1.298	1.289(7)	1.295	1.302	1.294	1.303(6)
C(7)–O(4)	1.215	1.220	1.215	1.206(7)	1.216	1.220	1.211	1.208(6)
C(13)–O(5)	1.294	1.300	1.294	1.286(7)	1.292	1.299	1.294	1.267(6)
C(13)–O(6)	1.216	1.221	1.216	1.220(7)	1.217	1.221	1.209	1.222(6)
Bond angles								
N(1)–M–O(1)	80.35	79.96	80.43	80.44(15)	81.07	80.65	81.54	81.15(14)
N(2)–M–O(3)	80.32	79.89	80.40	81.27(17)	80.87	80.39	80.92	81.90(14)
N(3)–M–O(5)	80.32	79.94	80.40	80.72(16)	81.18	80.76	81.89	81.75(15)
N(1)–M–N(3)	170.55	170.09	170.70	170.95(17)	170.50	169.93	169.06	170.73(16)
N(2)–M–O(5)	175.27	174.91	175.41	172.52(18)	174.85	174.45	175.93	172.48(15)
O(1)–M–O(3)	176.47	176.01	176.47	179.46(15)	175.88	175.39	173.47	179.07(14)

Table 2 Frontier molecular orbital (FMO) energy levels

	mPW1PW91		B3LYP		PBE0	
	ε (eV)	Character (%)	ε (eV)	Character (%)	ε (eV)	Character (%)
mer-Ir(pic)$_3$						
L + 3	−1.608	99%$\pi^\star_{pic}$	−1.755	99% $\pi^\star_{pic}$	−1.598	99% $\pi^\star_{pic}$
L + 2	−2.053	97% $\pi^\star_{pic}$	−2.203	97% $\pi^\star_{pic}$	−2.031	97% $\pi^\star_{pic}$
L + 1	−2.121	97% $\pi^\star_{pic}$	−2.263	97% $\pi^\star_{pic}$	−2.102	97% $\pi^\star_{pic}$
LUMO	−2.206	99% $\pi^\star_{pic}$	−2.344	99% $\pi^\star_{pic}$	−2.188	99% $\pi^\star_{pic}$
$\Delta\varepsilon$	4.567		4.485		4.537	
HOMO	−6.929	58% d_{Ir} + 42%π_{pic}	−6.626	58% d_{Ir} + 42% π_{pic}	−6.887	58% d_{Ir} + 42% π_{pic}
H-1	−7.133	58% d_{Ir} + 42% π_{pic}	−6.833	59% d_{Ir} + 41% π_{pic}	−7.093	58% d_{Ir} + 42% π_{pic}
H-2	−7.366	59% d_{Ir} + 41% π_{pic}	−7.070	60% d_{Ir} + 40% π_{pic}	−7.327	59% d_{Ir} + 41% π_{pic}
H-3	−7.981	98% π_{pic}	−7.612	98% π_{pic}	−7.938	98% π_{pic}
H-4	−8.055	97%π_{pic}	−7.684	96%π_{pic}	−8.012	97% π_{pic}
mer-Rh(pic)$_3$						
L + 3	−1.776	61% d_{Rh} + 39% $\pi^\star_{pic}$	−2.101	61% d_{Rh} + 39% $\pi^\star_{pic}$	−1.735	61% d_{Rh} + 39% $\pi^\star_{pic}$
L + 2	−2.042	98% $\pi^\star_{pic}$	−2.194	98% $\pi^\star_{pic}$	−2.021	98% $\pi^\star_{pic}$
L + 1	−2.108	99% $\pi^\star_{pic}$	−2.252	99% $\pi^\star_{pic}$	−2.088	99% $\pi^\star_{pic}$
LUMO	−2.177	98% $\pi^\star_{pic}$	−2.314	98% $\pi^\star_{pic}$	−2.158	98% $\pi^\star_{pic}$
$\Delta\varepsilon$	5.336		4.863		5.306	
HOMO	−7.513	57% π_{pic} + 43% d_{Rh}	−7.177	56% π_{pic} + 44% d_{Rh}	−7.464	57% π_{pic} + 43% d_{Rh}
H-1	−7.705	61% π_{pic} + 39% d_{Rh}	−7.372	60% π_{pic} + 40% d_{Rh}	−7.658	61% π_{pic} + 39% d_{Rh}
H-2	−7.880	81% π_{pic} + 19% d_{Rh}	−7.541	85% π_{pic} + 15% d_{Rh}	−7.833	80% π_{pic} + 20% d_{Rh}
H-3	−7.972	95% π_{pic}	−7.610	92% π_{pic}	−7.929	95% π_{pic}
H-4	−8.139	73% π_{pic} + 27% d_{Rh}	−7.781	70% π_{pic} + 30% d_{Rh}	−8.096	73% π_{pic} + 27% d_{Rh}

Frontier molecular orbitals

It is important to study the characteristics of FMOs of the complexes to infer the nature of the electronic excitations that participate in optical transitions. The energy levels and composition of FMOs, as well as energy gaps between HOMO and LUMO, of the studied complexes are given in Table 2 and illustrated in Fig. 1. Adopting a pseudo-octahedral symmetry, the five degenerate energy levels of the d-metal orbitals split into a set of unoccupied molecular orbitals and a set of occupied molecular orbitals, which have a large contribution of d-orbitals. It has been reported that the HOMO eigenvalues predicted by hybrid functionals are generally better than those predicted by non-hybrid functionals, and are relatively sensitive to the fraction of HF exchange in the exchange-correlation functional [43]. Unfortunately, we have not found any experimental data on HOMO eigenvalues of complexes **1** and **2** to compare our results. Table 2 shows that mPW1PW91 and PBE0 with the same HF exchange fraction (25%) give a lower HOMO energy than B3LYP, which has a lower HF exchange fraction (20%). The trend of the HOMO energy is mPW1PW91 (−6.929 eV) < PBE0 (−6.887 eV) < B3LYP

(−6.626 eV) for complex **1** and mPW1PW91 (−7.513 eV) < PBE0 (−7.464 eV) < B3LYP (−7.177 eV) for complex **2**. It is known that LUMO eigenvalues calculated with hybrid functionals have no physical meaning, and fail to predict experimental data [43, 44]. However, their analysis is useful for determining energy gaps. LUMO energies of complexes **1** and **2** computed with mPW1PW91 and PBE0 are very close, and higher than those computed with B3LYP. LUMO orbital energies of iridium complex computed with each functional are close to those of rhodium complex, because the LUMO of complexes **1** and **2** are composed with negligible proportion of d-metal orbital. Contrary to LUMO, HOMO orbitals of complexes **1** and **2** are composed with a significant proportion of d-metal, while $4d_{Rh}$ orbitals are lower in energy than $5d_{Ir}$ orbitals, so the HOMO energies of rhodium complex are clearly lower than those of iridium complex.

Therefore, calculated energy gaps of mer-Rh(pic)$_3$ complex are larger than those of mer-Ir(pic)$_3$ complex. Computed energy gaps are classified in decreasing order $\Delta\varepsilon_{mPW1PW91} > \Delta\varepsilon_{PBE0} > \Delta\varepsilon_{B3LYP}$, with slight difference between mPW1PW91 and PBE0. All hybrid functionals show
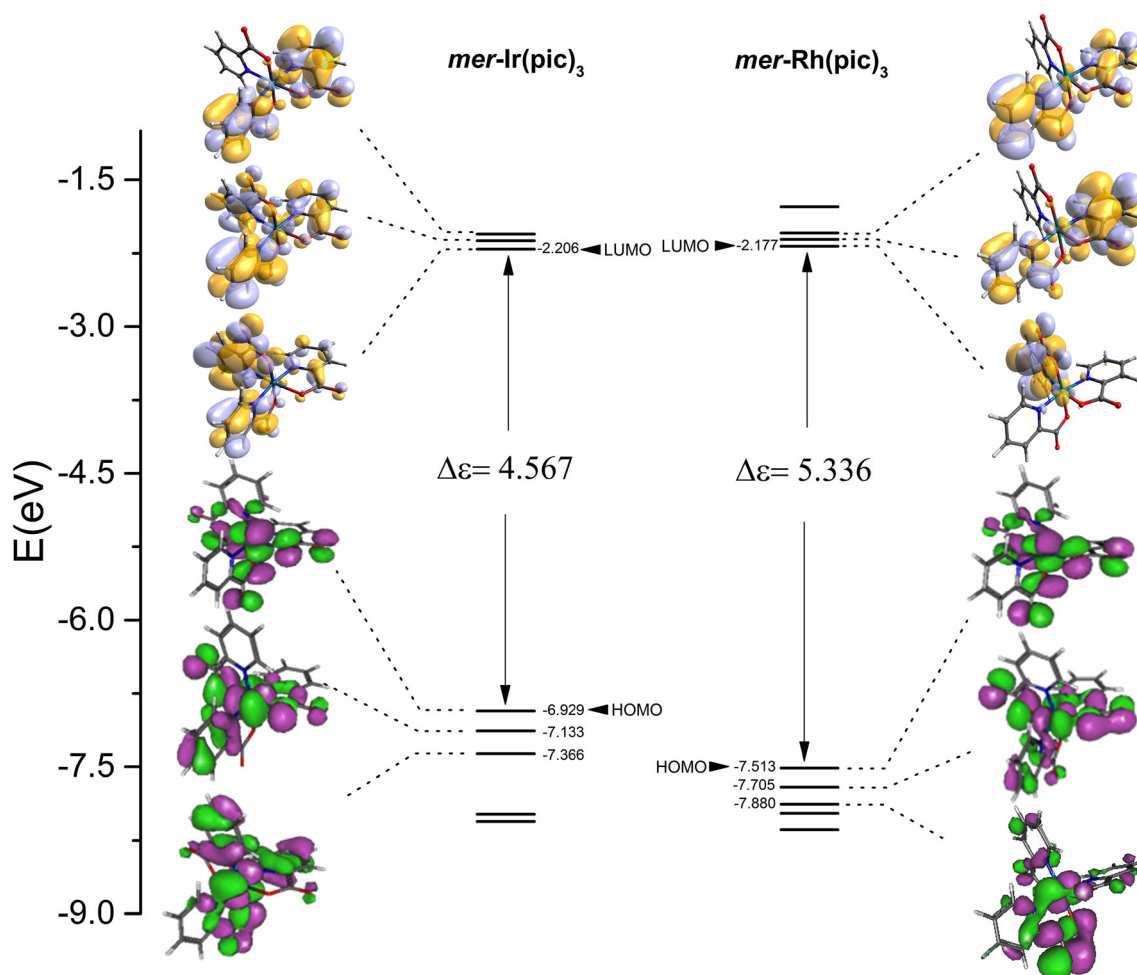
Fig. 1 Frontier molecular orbital (FMO) diagram of meridional (mer)-Ir(pic)$_3$ and mer-Rh(pic)$_3$ obtained with mPW1PW91

that HOMO, H-1 and H-2 of complex **1** have similar contribution of d$_{Ir}$ orbitals (58–60%) and similar contribution of π_{pic} orbitals (40–42%). The other lowest occupied orbitals (H-3···H-8) are delocalized over π_{pic} orbitals (Table S1). For complex **2**, the contribution of π_{pic} in HOMO and H-1 orbitals is more important than that of d$_{Rh}$ orbitals, mPW1PW91 and PBE0 give exactly the same composition. In H-2 and H-4 orbitals, the proportion of d$_{Rh}$ orbitals is smaller still (Table 2). The H-3 orbital resides mainly on π_{pic} orbitals (92–95%). The lowest unoccupied orbitals of the two complexes are delocalized on picolinate ligands, except that L + 3, L + 5 of mer-Ir(pic)$_3$ and L + 6, L + 7 of mer-Rh(pic)$_3$ are composed with a mixed proportion of d-metal orbitals and $\pi_{pic}^{\star}$ orbitals, this predicts d–d electronic excitations leading to metal-centered (MC) transition in the absorption spectra.

Electronic absorption spectra

Vertical TD-DFT transition energies and dipole transition moments of the lowest 80 singlet excited states of **1–2** were computed on the electronic ground state optimized geometries in acetonitrile with the same functionals and basis sets. Vertical transition energies to the lowest singlet excited states with significant oscillator strengths, and their characters calculated with mPW1PW91 and B3LYP are listed in Tables 3 and 4. Results obtained with PBE0 are reported in Table S3. All electronic spectra of **1–2** were simulated with a Gaussian function with full width at half maximum (FWHM) equal to 2660 cm^{-1}, and are depicted in Figs. 2 and 3 together with experimental data.

As reported by Basu et al. [20], experimental electronic spectra of complexes **1–2** in acetonitrile show one intense absorption below 400 nm (Figs. 1 and 2). The theoretical electronic spectra of mer-Ir(pic)$_3$ and mer-Rh(pic)$_3$ agree with experimental data, with all transitions calculated in UV region between 220 nm and 400 nm, and no absorption in the visible region due to the large energy gap of 4.485 eV for **1** and −7.177 eV for **2**, at the B3LYP level. This is in agreement with our previous study [45], where we found that the Ir(ppy)$_3$ complex energy gap of 3.456 eV (B3LYP) absorbs in the visible region.

Table 3 Time-dependent density functional theory (TD-DFT)/mPW1PW91 transition energies to the low-lying singlet states with significant oscillator strengths, the main configurations and the characters of the complexes mer-Ir(pic)$_3$ and mer-Rh(pic)$_3$

mPW1PW91

State	mer-Ir(pic)$_3$				State	mer-Rh(pic)$_3$			
	λ/nm	f	Transition	Character		λ/nm	f	Transition	Character
S$_1$	341	0.0007	HOMO → LUMO (75%)	MLCT/LLCT	S$_1$	384	0.0017	HOMO → L + 3 (79%)	MLCT/LLCT/MC
			HOMO → L + 1 (19%)						
S$_2$	330	0.0182	HOMO → L + 1 (76%)	MLCT/LLCT	S$_2$	355	0.0013	H-1 → L + 3 (61%)	MLCT/LLCT/MC
			HOMO → LUMO (20%)					H-1 → L + 5 (13%)	
S$_3$	323	0.0126	HOMO → L + 2 (86%)	MLCT/LLCT	S$_{10}$	280	0.0104	H-1 → L + 1 (16%)	MLCT/LLCT
								H-1 → LUMO (12%)	
								H-3 → LUMO (10%)	
S$_4$	320	0.0049	H-1 → L + 1 (47%)	MLCT/LLCT/MC	S$_{11}$	278	0.0113	H-3 → LUMO (18%)	MLCT/LLCT
			H-1 → L + 2 (14%)					HOMO → LUMO (16%)	
			HOMO → L + 6 (25%)					H-1 → LUMO (14%)	
S$_5$	318	0.0113	H-1 → LUMO (83%)	MLCT/LLCT	S$_{13}$	269	0.0107	H-5 → LUMO (11%)	MLCT/LLCT
								H-3 → LUMO (16%)	
								H-1 → LUMO (61%)	
					S$_{14}$	264	0.035	H-1 → L + 2 (41%)	MLCT/LLCT
								H-1 → L + 1 (29%)	
S$_7$	302	0.1159	H-1 → L + 2 (73%)	MLCT/LLCT	S$_{15}$	262	0.0156	H-1 → L + 2 (41%)	MLCT/LLCT
			H-1 → L + 1 (12%)					H-3 → L + 1 (15%)	
								H-5 → L + 1 (10%)	
S$_8$	300	0.0139	H-2 → LUMO (18%)	MLCT/LLCT	S$_{16}$	255	0.0499	H-4 → LUMO (21%)	MLCT/LLCT
			H-2 → L + 1 (30%)						
			H-2 → L + 2 (42%)					H-2 → LUMO (52%)	
S$_{10}$	294	0.1070	H-2 → LUMO (63%)	MLCT/LLCT	S$_{17}$	253	0.0245	H-4 → L + 1 (25%)	MLCT/LLCT
								H-4 → L + 2 (11%)	
			H-2 → L + 2 (21%)					H-3 → L + 1 (13%)	
S$_{12}$	284	0.0470	H-2 → L + 1 (57%)	MLCT/LLCT	S$_{20}$	242	0.016	H-3 → L + 3 (27%)	MLCT/LLCT/LMCT
								H-2 → L + 3 (11%)	
			H-2 → L + 2 (21%)					H-1 → L + 4 (15%)	
S$_{21}$	260	0.0261	H-2 → L + 3 (69%)	MLCT/LLCT	S$_{21}$	241	0.0224	H-1 → L + 4 (40%)	MLCT/LLCT/LMCT
			H-1 → L + 4 (16%)					H-3 → L + 3 (18%)	
S$_{22}$	259	0.0182	H-2 → L + 3 (14%)	MLCT/LLCT	S$_{22}$	239	0.0184	H-3 → L + 1 (12%)	LLCT
			H-1 → L + 4 (65%)						
S$_{23}$	255	0.0122	H-2 → L + 6 (36%)	MC/MLCT/LLCT	S$_{24}$	239	0.0232	HOMO → L + 6 (17%)	MLCT/LLCT/LMCT
								H-5 → L + 3 (11%)	
								H-4 → L + 3 (11%)	
								H-1 → L + 4 (10%)	
			H-1 → L + 7 (35%)		S$_{25}$	238	0.0115	H-3 → L + 2 (20%)	LLCT
								H-5 → LUMO (11%)	
S$_{33}$	230	0.0676	H-6 → LUMO (38%)	LLCT	S$_{26}$	238	0.0328	HOMO → L + 6 (29%)	LLCT/MLCT/MC
			H-6 → L + 2 (17%)						
			H-5 → L + 2 (10%)					H-3 → L + 2 (10%)	
S$_{35}$	228	0.1153	H-5 → L + 2 (20%)	LLCT	S$_{33}$	232	0.0536	H-3 → L + 3 (17%)	LLCT/LMCT
			H-6 → LUMO (18%)						
			H-6 → L + 1 (15%)						
			H-6 → L + 2 (15%)						
S$_{38}$	227	0.0406	H-7 → LUMO (35%)	LLCT	S$_{35}$	231	0.0294	H-3 → L + 5 (41%)	LLCT/LMCT/MLCT/MC
			H-7 → L + 1 (29%)					H-2 → L + 5 (17%)	
			H-6 → L + 1 (11%)					H-1 → L + 6 (14%)	
S$_{39}$	225	0.1479	H-8 → LUMO (55%	LLCT	S$_{37}$	230	0.016	H-5 → L + 3 (10%)	LMCT/MLCT/LLCT

Table 3 (continued)

mPW1PW91

State	mer-Ir(pic)$_3$				State	mer-Rh(pic)$_3$			
	λ/nm	f	Transition	Character		λ/nm	f	Transition	Character
								H-3 → L + 4 (17%)	
								H-1 → L + 6 (10%)	
S$_{42}$	223	0.0436	H-9 → L + 1 (18%)	LLCT	S$_{41}$	227	0.0289	H-7 → LUMO (15%)	LLCT/LMCT
			H-7 → L + 1 (16%)					H-3 → L + 4 (20%)	
			H-7 → L + 2 (10%)		S$_{47}$	221	0.1054	H-1- > L + 7 (30%)	LLCT/LMCT
								H-7- > L + 2 (11%)	

Electronic spectra of **1-2** complexes simulated with mPW1PW91 and PBE0 are quasi-superimposed and characterized by three absorption bands, the first obtained at ~298 nm with average intensity, the second obtained at ~259 nm with a low intensity, and a most intense band in the UV-C region calculated at ~227 nm. The two functionals show that complexes **1** and **2** begin to absorb at ~375 nm and ~372 nm, respectively. B3LYP gives the similar absorption band characteristics to those of mPW1PW91 and PBE0, with a shift to the red. Since mPW1PW91 and PBE0 give very similar results, we will discuss and compare only the results obtained with mPW1PW91 and B3LYP. The first absorptions (S$_0$–S$_1$) of complexes **1** and **2** are calculated at 384 nm and 341 nm, respectively, with mPW1PW91, despite the energy gap in the rhodium complex being larger as compared to that of the iridium complex. In contrast to the iridium complex, the first transition of the rhodium complex corresponds to a π_{pic}+ $d_{Rh} \rightarrow d_{Rh} + \pi^\star_{pic}$ excitation leading to a state with significant MC character requiring low energy with a modest oscillator strength ($f = 0.0007$). This S$_0$–S$_1$ absorption is assigned to the lowest band observed near ~370 nm in both complexes. In the UV-B region, several excited states were calculated, with the different functionals have mixed MLCT/LLCT character, with various oscillator strengths. The two absorptions (S$_0$–S$_7$, $f = 0.1159$) and (S$_0$–S$_{10}$, $f = 0.1070$) of complex **1** calculated with mPW1PW91, with significant oscillator strengths, corresponding to $d_{Ir} + \pi_{pic} \rightarrow \pi^\star_{pic}$ excitation, can be assigned to the band observed at 296 nm. The band of medium intensity observed at 270 nm can be assigned to the S$_0$–S$_{21}$ absorption ($f = 0.0261$) calculated at 260 nm with mPW1PW91, which corresponds to $d_{Ir} + \pi_{pic} \rightarrow \pi^\star_{pic}$ and has MLCT/LLCT mixed character.

The most intense band observed at 236 nm in the spectrum of **1** is assigned to S$_0$–S$_{39}$ ($f = 0.1479$) absorption purely LLCT calculated at 225 nm with mPW1PW91 and corresponding to a $\pi_{pic} \rightarrow \pi^\star_{pic}$ excitation. With B3LYP this band is also assigned to a $\pi_{pic} \rightarrow \pi^\star_{pic}$ excitation (S$_0$–S$_{42}$, $f = 0.1601$) calculated at 234 nm. We assigned the band observed at

266 nm in complex **2** spectrum to the S$_0$–S$_{16}$ transition calculated at 255 nm mPW1PW91 corresponding to $d_{Rh} + \pi_{pic} \rightarrow \pi^\star_{pic}$ excitation with significant oscillator strength $f = 0.0499$. The intense band observed in the UV-C region of the rhodium complex spectrum at 218 nm is assigned to the S$_0$–S$_{47}$ transition calculated at 221 nm with mPW1PW91, which has a mixed LLCT/MLCT character, and is characterized by an important intraligand $\pi_{pic} \rightarrow \pi^\star_{pic}$ excitation. The presence of LMCT (ligand to metal charge transfer) states mixed with MC, MLCT and LLCT characterizes the rhodium complex spectrum in contrast to the iridium complex spectrum. This difference is due to the presence of d-unoccupied orbitals (L + 3) at low energy in the rhodium complex leading to MC and LMCT transitions. The absorption spectra of these complexes, which are characterized by the presence of low-lying singlet and triplet MC states, are affected by SOC effects [46].

Infra-red spectra

Figures 4 and 5 report the comparison of the experimental IR spectra reported in [15] of the studied complexes in acetonitrile with the IR intensity calculated for each complex. In order to allow for a better comparison, three spectra performed using the B3LYP, PBE0 and mPW1PW91 functionals are plotted on the same spectral scale. As illustrated in Figs. 4 and 5, the calculated IR spectra show similar features by using three different hybrid functionals, especially, a very good agreement between PBE0. mPW1PW91 functionals. The IR spectra of two complexes appear very similar.

In both IR spectra, four bands are calculated, the weak bands at 457 cm^{-1} for mer-Ir(pic)$_3$ and 463 cm^{-1} for mer-Rh(pic)$_3$ respectively, correspond to (O-C-O) of carboxylate ring [47], the second band centered around 700 cm^{-1} for mer-Ir(pic)$_3$ is assigned to C–C–C stretching of picolinate groups also, the peaks located at 791 cm^{-1} for mer-Rh(pic)$_3$ is attributed to symmetric and asymmetric C-H stretching modes of the three aromatic ring in picolinate groups [48]. The C = C

Table 4 TD-DFT/B3LYP transition energies (in cm^{-1} and nm) to the low-lying singlet states with significant oscillator strengths, the main configurations and the characters of the complexes mer-Ir(pic)$_3$ and mer-Rh(pic)$_3$

B3LYP

State	mer-Ir(pic)$_3$				State	mer-Rh(pic)$_3$			
	λ/nm	f	Transition	Character		λ/nm	f	Transition	Character
S_1	362	0.0009	HOMO → LUMO (80%)	MLCT/LLCT	S_1	402	0.0017	HOMO → L + 3 (78%)	LLCT/MLCT/MC
			HOMO → L + 1 (16%)					HOMO → L + 4 (8%)	
S_2	351	0.016	HOMO → LUMO (17%)	MLCT/LLCT	S_2	373	0.0013	H-1 → L + 3 (63%)	LLCT/MLCT/MC
			HOMO → L + 1 (80%)					H-1 → L + 4 (17%)	
S_7	320	0.1035	H-1 → L + 2 (76%)	MLCT/LLCT	S_{14}	280	0.0315	H-1 → L + 2 (55%)	LLCT/MLCT
			H-1 → L + 1 (11%)					H-1 → L + 1 (21%)	
S_8	316	0.0127	H-2 → L + 2 (43%)	MLCT/LLCT	S_{16}	269	0.0339	H-2 → LUMO (48%)	LLCT/MLCT
			H-2 → L + 1 (28%)					H-4 → LUMO (19%)	
			H-2 → LUMO (22%)					H-3 → LUMO (11%)	
S_{10}	309	0.096	H-2 → LUMO (61%)	MLCT/LLCT	S_{20}	263	0.0431	H-2 → L + 3 (45%)	LLCT/MLCT/LMCT
								H-3 → L + 3 (19%)	
			H-2 → L + 2 (25%)					H-4 → L + 3 (15%)	
S_{12}	298	0.0493	H-2 → L + 1 (63%)	MLCT/LLCT	S_{24}	255	0.0357	H-3 → L + 2 (24%)	LLCT/LMCT
								H-3 → L + 4 (15%)	
			H-2 → L + 2 (21%)					H-5 → LUMO (13%)	
S_{22}	272	0.0353	H-2 → L + 3 (70%)	MLCT/LLCT	S_{30}	252	0.0239	H-6 → L + 3 (19%)	LLCT/LMCT
			H-1 → L + 4 (15%)					H-9 → L + 3 (7%)	
S_{36}	240	0.0263	H-6 → L + 1 (75%)	LLCT	S_{38}	243	0.0208	H-1 → L + 7 (24%)	MLCT/LLCT
								H-2 → L + 5 (21%)	
S_{38}	238	0.0561	H-6 → L + 2 (65%)	LLCT	S_{43}	240	0.037	H-3 → L + 5 (27%)	LLCT/MLCT
								H-1 → L + 7 (16%)	
S_{41}	235	0.0306	H-8 → LUMO (47%)	LLCT	S_{49}	236	0.0333	H-6 → L + 2 (46%)	LMCT/LLCT
			H-8 → L + 1 (20%)					H-9 → L + 2 (15%)	
								H-6 → L + 4 (11%)	
S_{42}	234	0.1601	H-7 → L + 1 (50%)	LLCT	S_{55}	232	0.0629	H-7 → L + 2 (13%)	LMCT/LLCT/MLCT
								H-7 → L + 4 (13%)	
								H-1 → L + 6 (10%)	
								H-1 → L + 7 (14%)	
S_{43}	233	0.0524	H-8 → L + 1 (53%)	LLCT	S_{56}	231	0.01	H-9 → L + 4 (26%)	LLCT/LMCT
								H-8 → L + 4 (12%)	
			H-9 → LUMO (20%)					H-6 → L + 4 (11%)	
S_{44}	232	0.0248	H-9 → LUMO (32%)	LLCT	S_{57}	231	0.0186	H-8 → LUMO (25%)	LLCT/LMCT
			H-7 → L + 2 (26%)					H-9 → L + 4 (13%)	
			H-9 → L + 1 (18%)					H-8 → L + 4 (11%)	
S_{45}	232	0.0661	H-9 → LUMO (32%)	LLCT	S_{58}	230	0.052	H-8 → L + 2 (25%)	LLCT/MLCT
			H-8 → LUMO (12%)						
			H-7 → L + 2 (12%)					H-2 → L + 5 (10%)	
S_{50}	225	0.0408	H-4 → L + 3 (35%)	LLCT	S_{60}	229	0.0138	H-8 → L + 2 (18%)	LLCT/MLCT
			H-4 → L + 4 (10%)					H-2 → L + 5 (13%)	
			H-3 → L + 3 (12%),					H-2 → L + 6 (12%)	

and C = N stretching frequencies were calculated in the range of 1330 cm^{-1} and 1360 cm^{-1} for both mer-Ir(pic)$_3$ and mer-Rh(pic)$_3$ [40]. Several peaks are calculated in the interval 1600–1730 cm^{-1} with all functionals. The peak calculated with B3LYP at 1606 cm^{-1} and at 1609 cm^{-1} for complexes **1** and **2** respectively, is attributed to C–C stretching, and ring deformation in the pyridine. The peak calculated with B3LYP

at 1648 cm^{-1} for complex **1** and at 1644 cm^{-1} for complex **2**, of average intensity, corresponds also to the pyridine ring vibrations; this result agrees with previous studies [49, 50]. The strong peak calculated with B3LYP at 1717 cm^{-1} for mer-Ir(pic)$_3$ and 1734 cm^{-1} for mer-Rh(pic)$_3$, corresponds to asymmetric CO stretching vibrations of carboxylate fragment bonded to the pyridine; this result also agrees with previously
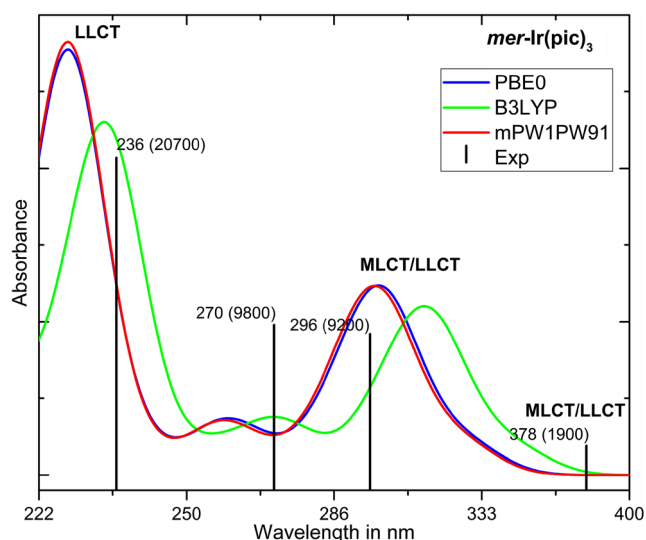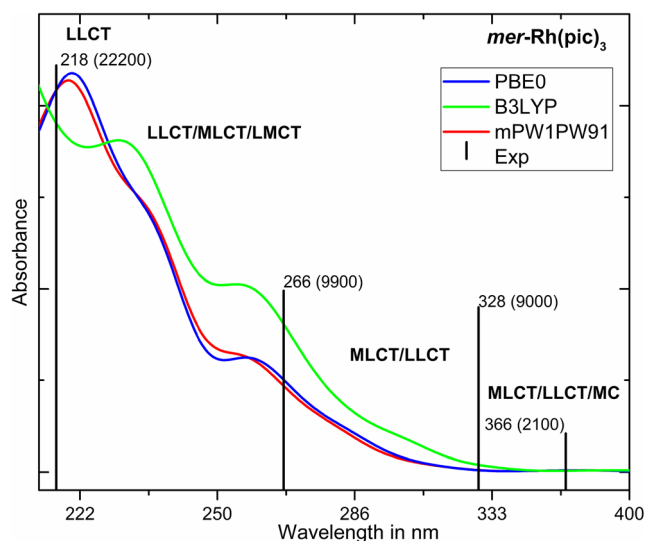
Fig. 2 Simulated absorption spectra and most significant observed absorptions of mer-Ir(pic)$_3$. Observed absorption energies are given in nm with the corresponding intensities in brackets (from [20])

reported data [48, 51]. All absorptions calculated in the range 1600–1730 cm^{-1} can be assigned to the broad and strong band observed at 1684 cm^{-1} in mer-Ir(pic)$_3$ and at 1676 cm^{-1} in mer-Rh(pic)$_3$.

Conclusions

In this work, the structures, FMOs, UV and IR absorption spectra of complexes **1** and **2** have been computed by means DFT and TD-DFT methods. Calculated structural parameters agree with experimental data, except for the Ir-N bond lengths, which are slightly longer than X-ray values. LUMO energy

Fig. 3 Simulated absorption spectra and most significant observed absorptions of mer-Rh(pic)$_3$. Observed absorption energies are given in nm with the corresponding intensities in brackets (from [20])
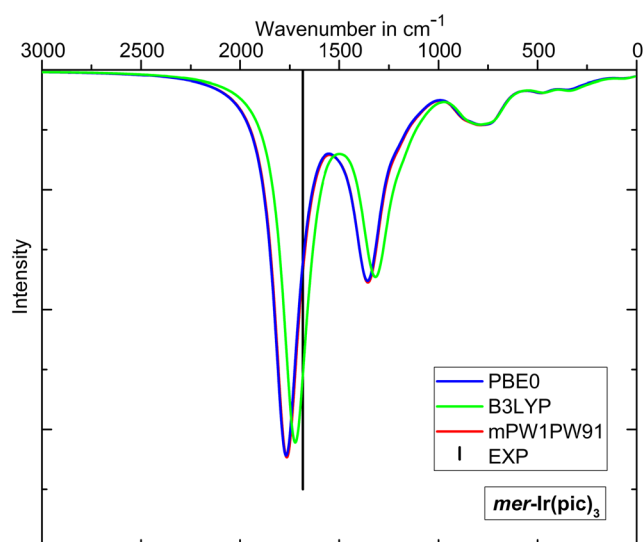
Fig. 4 Simulated infra red (IR) spectra of mer-Ir(pic)$_3$. *Black bar* Wavenumber of the broad and strong band observed (from [20])

levels of iridium and rhodium complexes are very close, and are all delocalized over $\pi^{\star}_{pic}$ orbitals. HOMO energy levels of the rhodium complex are lower than those of iridium complex, therefore energy gaps of mer-Rh(pic)$_3$ complex are larger than those of mer-Ir(pic)$_3$ complex. HOMO orbitals of both complexes correspond to the d-metal orbitals and π_{pic}orbitals. The electronic absorption spectra show that all absorptions calculated in UV region between 220 and 400 nm and do not show any absorption in the visible region due to large energy gaps. PBE0 and mPW1PW91, which have the same HF exchange fraction (25%) give very similar absorption spectra and differ slightly from B3LYP, which has 20% of HF exchange. The lowest singlet states correspond to MLCT/LLCT in complex **1** and to MLCT/LLCT/MC mixed character in complex **2**. The
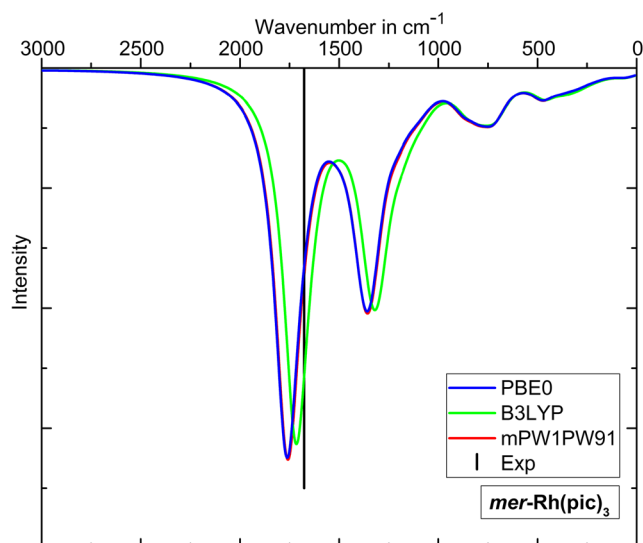

Fig. 5 Simulated IR spectra of mer-Rh(pic)$_3$. *Black bar* Wavenumber of the broad and strong band observed (from [20])

most intense band observed at 236 nm (complex **1**) and 218 nm (complex **2**) have been assigned to LLCT states, which correspond to $\pi_{pic} \to \pi_{pic}^{\star}$ transitions. The presence of virtual d-rhodium orbitals in low orbital energy levels lead to low-lying MC excited states (d–d transition), which play a crucial role in photochemical properties. The occurrence of picolinate as bidentate ligands by our theoretically computed wavenumbers gives rise to specific bands at 1717 cm^{-1} for mer-Ir(pic)$_3$ and 1734 cm^{-1} for mer-Rh(pic)$_3$ in IR spectra, which indicates the asymmetric vibration of carboxylate on the aromatic ring of picolinate.

References

1. Alagona G, Ghio C, Rocchiccioli S (2007) Computational prediction of the regio- and diastereoselectivity in a rhodium-catalyzed hydroformylation/cyclization domino process. J Mol Model 13: 823–837. https://doi.org/10.1007/s00894-007-0205-8

2. Xu S, Wang J, Xia H, Zhao F and Wang Y (2015) Computational prediction for emission energy of iridium (III) complexes based on TDDFT calculations using exchange-correlation functionals containing various HF exchange percentages. J Mol Model 21:22. https://doi.org/10.1007/s00894-014-2557-1

3. Zhang T-T, Qi X-X, Jia J, Wu H-S (2012) Tuning electronic structure and photophysical properties of [Ir(ppy)2(py)2]+ by substituents binding in pyridyl ligand: a computational study. J Mol Model 18:4615–4624. https://doi.org/10.1007/s00894-012-1462-8

4. Chen M, Serna P, Lu J, Gates BC, Dixon DA (2015) Molecular models of site-isolated cobalt, rhodium, and iridium catalysts supported on zeolites: ligand bond dissociation energies. Comput Theor Chem 1074:58–72. https://doi.org/10.1016/j.comptc.2015.09.004

5. Meng Q, Shen W, Li M (2011) Mechanism of intermolecular hydroacylation of vinylsilanes catalyzed by a rhodium(I) olefin complex: a DFT study. J Mol Model 18:1229–1239. https://doi.org/10.1007/s00894-011-1151-z

6. Ahn SY, Ha Y (2009) The blue phosphorescent iridium complexes containing new triazole ligands for OLEDs. Mol Cryst Liq Cryst 504:59–66. https://doi.org/10.1080/15421400902939504

7. Morello G R (2017) Accurate prediction of emission energies with TD-DFT methods for platinum and iridium OLED materials. J Mol Model 23:174. https://doi.org/10.1007/s00894-017-3348-2

8. Park HR, Ha Y (2012) Comparison of emission characteristics with 4-, 5-, 6-membered iridium complexes for OLEDs. Mol Cryst Liq Cryst 563:246–256. https://doi.org/10.1080/15421406.2012.689729

9. Park S-Y, Kim H-K, Shin D-M (2016) Synthesis and characterization of red phosphorescent iridium(III) complexes based on electron-acceptor modulation of main ligand for high efficiency organic light-emitting diodes. Mol Cryst Liq Cryst 636:38–44. https://doi.org/10.1080/15421406.2016.1200941

10. Simpson PV, Schmidt C, Ott I, Bruhn H, Schatzschneider U (2013) Synthesis, cellular uptake and biological activity against pathogenic microorganisms and cancer cells of rhodium and iridium N-heterocyclic carbene complexes bearing charged substituents. Eur J Inorg Chem 2013:5547–5554. https://doi.org/10.1002/ejic.201300820

11. Almodares Z, Lucas SJ, Crossley BD, Basri AM, Pask CM, Hebden AJ, Phillips RM, McGowan PC (2014) Rhodium, iridium, and ruthenium half-sandwich picolinamide complexes as anticancer agents. Inorg Chem 53:727–736. https://doi.org/10.1021/ic401529u

12. Leung C-H, Zhong H-J, Chan DS-H, Ma D-L (2013) Bioactive iridium and rhodium complexes as therapeutic agents. Coord Chem Rev 257: 1764–1776. https://doi.org/10.1016/j.ccr.2013.01.034

13. Seth SK, Mandal S, Purkayastha P, Gupta P (2015) Cyclometalated mono and dinuclear rhodium(III) and iridium(III) complexes with imidazolyl phenanthrolines: synthesis and, photophysical and electrochemical characterization. Polyhedron 95:14–23. https://doi.org/10.1016/j.poly.2015.04.011

14. Jayabharathi J, Jayamoorthy K, Thanikachalam V (2014) Synthesis, photophysical and electroluminescent properties of green organic light emitting devices based on novel iridium complexes containing benzimidazole ligands. J Organomet Chem 761: 74–83. https://doi.org/10.1016/j.jorganchem.2014.03.002

15. Xu J-X, Xue H, Zou H, Ke S-W, Qin T, Wang X, Shen X, Zhu D-R (2016) Syntheses and characterizations of 5-nitro-2-(3′,5′-di(trifluoromethyl)phenyl)pyridyl-containing iridium(III) complexes and the two-band white photoluminescence properties in solution. J Coord Chem 69:3172–3181. https://doi.org/10.1080/00958972.2016.1230671

16. Yi S, Kim J-H, Cho Y-J, Lee J, Choi T-S, Cho DW, Pac C, Han W-S, Son H-J, Kang SO (2016) Stable blue phosphorescence iridium(III) cyclometalated complexes prompted by intramolecular hydrogen bond in ancillary ligand. Inorg Chem 55:3324–3331. https://doi.org/10.1021/acs.inorgchem.5b02511

17. Minaev B, Minaeva V, Ågren H (2009) Theoretical study of the cyclometalated iridium(III) complexes used as chromophores for organic light-emitting diodes. J Phys Chem A 113:726–735. https://doi.org/10.1021/jp807429h

18. Minaev B, Baryshnikov G, Agren H (2014) Principles of phosphorescent organic light emitting devices. Phys Chem Chem Phys 16: 1719–1758. https://doi.org/10.1039/c3cp53806k

19. Ko S-B, Lu J-S, Kang Y, Wang S (2013) Impact of a picolinate ancillary ligand on phosphorescence and fluoride sensing properties of BMes2-functionalized platinum(II) compounds. Organometallics 32:599–608. https://doi.org/10.1021/om301112u

20. Basu S, Peng S-M, Lee G-H, Bhattacharya S (2005) Synthesis, structure and electrochemical properties of tris-picolinate complexes of rhodium and iridium. Polyhedron 24:157–163. https://doi.org/10.1016/j.poly.2004.10.015

21. Becke AD (1993) Density-functional thermochemistry. III. The role of exact exchange. J Chem Phys 98:5648. https://doi.org/10.1063/1.464913

22. Hohenberg P, Kohn W (1964) Inhomogeneous electron gas. Phys Rev 136:B864–B871. https://doi.org/10.1103/physrev.136.b864

23. Lee C, Yang W, Parr RG (1988) Development of the Colle-Salvetti correlation-energy formula into a functional of the electron density. Phys Rev B 37:785–789. https://doi.org/10.1103/physrevb.37.785

24. Adamo C, Barone V (1999) Toward reliable density functional methods without adjustable parameters: the PBE0 model. J Chem Phys 110:6158. https://doi.org/10.1063/1.478522

25. Adamo C, Barone V (1998) Exchange functionals with improved long-range behavior and adiabatic connection methods without adjustable parameters: the mPW and mPW1PW models. J Chem Phys 108:664. https://doi.org/10.1063/1.475428

26. Binning RC, Curtiss LA (1990) Compact contracted basis sets for third-row atoms: Ga-Kr. J Comput Chem 11:1206–1216. https://doi.org/10.1002/jcc.540111013

27. Krishnan R, Binkley JS, Seeger R, Pople JA (1980) Self-consistent molecular orbital methods. XX. A basis set for correlated wave functions. J Chem Phys 72:650. https://doi.org/10.1063/1.438955

28. McLean AD, Chandler GS (1980) Contracted Gaussian basis sets for molecular calculations. I. Second row atoms, Z=11–18. J Chem Phys 72:5639. https://doi.org/10.1063/1.438980

29. Hay PJ, Wadt WR (1985) Ab initio effective core potentials for molecular calculations. Potentials for the transition metal atoms Sc to Hg. J Chem Phys 82:270. https://doi.org/10.1063/1.448799

30. Hay PJ, Wadt WR (1985) Ab initio effective core potentials for molecular calculations. Potentials for K to Au including the outermost core orbitals. J Chem Phys 82:299. https://doi.org/10.1063/1.448975

31. Cancès E, Mennucci B, Tomasi J (1997) A new integral equation formalism for the polarizable continuum model: theoretical background and applications to isotropic and anisotropic dielectrics. J Chem Phys 107:3032. https://doi.org/10.1063/1.474659

32. Cossi M, Barone V, Mennucci B, Tomasi J (1998) Ab initio study of ionic solutions by a polarizable continuum dielectric model. Chem Phys Lett 286:253–260. https://doi.org/10.1016/s0009-2614(98)00106-7

33. Casida ME (1995) Time-dependent density functional response theory for molecules. In: Chong DP (ed) Recent advances in density functional methods, part I. World Scientific, Singapore, pp 155–192

34. Casida ME (1996) Time-dependent density functional response theory of molecular systems: theory, computational methods, and functionals. In: Seminario JM (ed) Recent developments and applications of modern density functional theory. Elsevier, Amsterdam, pp 391–439

35. Runge E, Gross EKU (1984) Density-functional theory for time-dependent systems. Phys Rev Lett 52:997–1000. https://doi.org/10.1103/physrevlett.52.997

36. Frisch MJ, Trucks GW, Schlegel HB, Scuseria GE, Robb MA, Cheeseman JR, Scalmani G, Barone V, Mennucci B, Petersson GA, Nakatsuji H, Caricato M, Li X, Hratchian HP, Izmaylov AF, Bloino J, Zheng G, Sonnenberg JL, Hada M, Ehara M, Toyota K, Fukuda R, Hasegawa J, Ishida M, Nakajima T, Honda Y, Kitao O, Nakai H, Vreven T, Montgomery Jr JA, Peralta JE, Ogliaro F, Bearpark M, Heyd JJ, Brothers E, Kudin KN, Staroverov VN, Kobayashi R, Normand J, Raghavachari K, Rendell A, Burant JC, Iyengar SS, Tomasi J, Cossi M, Rega N, Millam JM, Klene M, Knox JE, Cross JB, Bakken V, Adamo C, Jaramillo J, Gomperts R, Stratmann RE, Yazyev O, Austin AJ, Cammi R, Pomelli C, Ochterski JW, Martin RL, Morokuma K, Zakrzewski VG, Voth GA, Salvador P, Dannenberg JJ, Dapprich S, Daniels AD, Foresman JB, Ortiz JV, Cioslowski J, Fox DJ (2009) Gaussian 09. Gaussian, Inc., Wallingford

37. O'Boyle NM, Tenderholt AL, Langner KM (2008) cclib: a library for package-independent computational chemistry algorithms. J Comput Chem 29:839–845. https://doi.org/10.1002/jcc.20823

38. Hanwell MD, Curtis DE, Lonie DC, Vandermeersch T, Zurek E, Hutchison GR (2012) Avogadro: an advanced semantic chemical editor, visualization, and analysis platform. J Cheminform 4:17. https://doi.org/10.1186/1758-2946-4-17

39. Farrugia LJ (2012) WinGXandORTEP for windows: an update. J Appl Crystallogr 45:849–854. https://doi.org/10.1107/s0021889812029111

40. Hakimi M (2013) Structural and spectral characterization of a chromium(III) picolinate complex: introducing a new redox reaction. J Korean Chem Soc 57:721–725. https://doi.org/10.5012/jkcs.2013.57.6.721

41. Li X, Zhang Q, Tu Y, Ågren H, Tian H (2010) Modulation of iridium (III) phosphorescence via photochromic ligands: a density functional theory study. Phys Chem Chem Phys 12:13730. https://doi.org/10.1039/c0cp00564a

42. Nie D, Liu Z, Bian Z, Huang C (2008) Assessment of density functionals for the investigation of iridium(III) complexes. J Mol Struct 861:97–102. https://doi.org/10.1016/j.theochem.2008.04.033

43. Zhang G, Musgrave CB (2007) Comparison of DFT methods for molecular orbital eigenvalue calculations. J Phys Chem A 111:1554–1561. https://doi.org/10.1021/jp061633o

44. Baerends EJ, Gritsenko OV, van Meer R (2013) The Kohn-Sham gap, the fundamental gap and the optical gap: the physical meaning of occupied and virtual Kohn-Sham orbital energies. Phys Chem Chem Phys 15:16408. https://doi.org/10.1039/c3cp52547c

45. Brahim H, Daniel C (2014) Structural and spectroscopic properties of Ir(III) complexes with phenylpyridine ligands: absorption spectra without and with spin-orbit-coupling. Comput Theor Chem 1040–1041:219–229. https://doi.org/10.1016/j.comptc.2014.01.030

46. Brahim H, Daniel C, Rahmouni A (2011) Spin-orbit absorption spectroscopy of transition metal hydrides: a TD-DFT and MS-CASPT2 study of HM(CO)5 (M = Mn, Re). Int J Quantum Chem 112:2085–2097. https://doi.org/10.1002/qua.23219

47. Tsai H-R, Lu K-Y, Lai S-H, Fan C-H, Cheng C-H, Chen IC (2011) Metal–ligand bonding strength of fluoro-substituted cyclometalated iridium(III) complexes from raman and infrared spectra. J Phys Chem C 115:17163–17174. https://doi.org/10.1021/jp204130a

48. Gipson K, Stevens K, Brown P, Ballato J (2015) Infrared spectroscopic characterization of photoluminescent polymer nanocomposites. J Spectrosc 2015:1–9. https://doi.org/10.1155/2015/489162

49. Gharah N, Drew MGB, Bhattacharyya R (2009) Synthesis and catalytic epoxidation potentiality of oxodiperoxo molybdenum(VI) complexes with pyridine-2-carboxaldoxime and pyridine-2-carboxylate: the crystal structure of PMePh3[MoO(O2)2(PyCO)]. Transition Met Chem (London) 34:549–557. https://doi.org/10.1007/s11243-009-9228-6

50. Hnatejko Z, Dutkiewicz G, Kubicki M, Lis S (2013) New complexes of cobalt(II) ions with pyridinecarboxylic acid N-oxides and 4,4′-byp. J Mol Struct 1034:128–133. https://doi.org/10.1016/j.molstruc.2012.08.044

51. Świderski G, Kalinowska M, Wojtulewski S, Lewandowski W (2006) Experimental (FT-IR, FT-Raman, 1H NMR) and theoretical study of magnesium, calcium, strontium, and barium picolinates. Spectrochim Acta A 64:24–33. https://doi.org/10.1016/j.saa.2005.06.034